Crystallization Process for High-Quality $Cs_{0.15}FA_{0.85}PbI_{2.85}Br_{0.15}$ Film Deposited via Simplified Sequential Vacuum Evaporation

Yan, Jin; Zhao, Jiashang; Wang, Haoxu; Kerklaan, Mels; Bannenberg, Lars J.; Ibrahim, Bahiya; Savenije, Tom J.; Mazzarella, Luana; Isabella, Olindo

DOI
10.1021/acsaem.3c00203

Publication date
2023

Document Version
Final published version

Published in
ACS Applied Energy Materials

ACS APPLIED ENERGY MATERIALS

www.acsaem.org

Forum Article

Crystallization Process for High-Quality $Cs_{0.15}FA_{0.85}PbI_{2.85}Br_{0.15}$ Film Deposited via Simplified Sequential Vacuum Evaporation

Jin Yan, Jiashang Zhao, Haoxu Wang, Mels Kerklaan, Lars J. Bannenberg, Bahiya Ibrahim, Tom J. Savenije,* Luana Mazzarella,* and Olindo Isabella

Cite This: https://doi.org/10.1021/acsaem.3c00203

Read Online

ACCESS | Metrics & More | Article Recommendations | Supporting Information

ABSTRACT: Multiple-source thermal evaporation is emerging as an excellent technique to obtain perovskite (PVK) materials for solar cell applications due to its solvent-free processing, accurate control of stoichiometric ratio, and potential for scalability. Nevertheless, the currently reported layer-by-layer deposition approach is afflicted by long processing times caused by the multiple repetitions of thin films, which hinder industrial uptake. On the other hand, the coevaporation entails higher complexity due to the challenges of controlling the sublimation of multiple sources simultaneously. In this work, we propose a simplified approach consisting of a single-cycle deposition (SCD) of three thick precursor layers to obtain high-quality $Cs_{0.15}FA_{0.85}PbI_{2.85}Br_{0.15}$ (CsFAPbIBr) films. After annealing, the optimized PVK film exhibits comparable properties to the one deposited by multicycle deposition in terms of crystal structure, in-depth uniformity, and optoelectrical properties. Also, the formation and evolution of SCD PVK during annealing are investigated. We found that, in the competitive processes of precursor diffusion and reaction, the presence of cesium bromide can assist precursor mixing driven by the annealing treatment, demonstrating a reaction-limited process in the PVK conversion. With this simplified SCD approach, a PVK film is obtained with expected optical and opto-electronic properties, providing an appealing way for future thermally evaporated PVK device preparation.

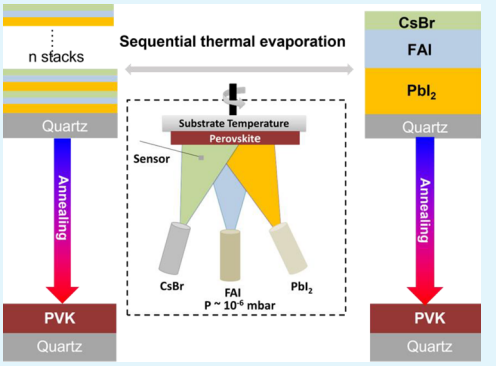

KEYWORDS: *$Cs_{0.15}FA_{0.85}PbI_{2.85}Br_{0.15}$, thermal evaporation, sequential vacuum evaporation, single-cycle deposition, postdeposition annealing*

INTRODUCTION

As a new absorber material for next-generation solar cells, metal halide perovskites (PVKs) have attracted intensive attention due to their high absorption coefficients,[1] long carrier diffusion lengths,[2] and apparent defect tolerance.[3] The rapid developments in material optimization and fabrication techniques have led to an unprecedented fast increase of the power conversion efficiency (PCE) of PVK solar cells (PSCs) exceeding 25% within a decade.[4] One of the key advancements in device PCE originates from the development of mixed-cation and mixed-halide PVKs, which improve the crystal structure and phase stability.[5] Nevertheless, some well-developed solution-based methods are still limited with respect to scalability because of low reproducibility and the use of hazardous solvents.[6] Vacuum deposition methods are possibly more attractive for device upscaling considering that they are widely employed in the semiconductor and silicon PV industries. Moreover, thermal evaporation is compatible with textured substrates.[6] Nevertheless, challenges still exist for high-quality PVK film preparation based on coevaporation, such as the realization of a stoichiometric composition[7] and achieving stable deposition rates for the methylammonium halide (MAX) precursors,[8] especially for multisource coevaporation. It has been shown that deposition of MAX and formamidinium halide (FAX) can lead to chamber pressure fluctuations during evaporation, affecting the deposition rate of other precursors and eventually the quality of the final PVK material. Li et al.[9] recently reported that the ratio of lead iodide (PbI_2) to methylammonium iodide (MAI) progressively increases with deposition time during coevaporation, resulting in a gradually changing composition as the PVK film grows. Instead of simultaneously controlling the rates of two or even more precursors during deposition, sequential deposition is less complex and allows for better stoichiometric control.[9] Feng et al.[10] used sequential deposition for the preparation of PVK films, and the resulting devices reached a PCE of 21.32% (0.1 cm^2). However, regarding thermally evaporated mixed-cation, mixed-halide PVK thin films, most of the reports are based on coevaporation,[11,12] while only a few sequential

Special Issue: Halide Perovskite Materials and Devices for Energy and Electronic Applications

Received: January 23, 2023
Accepted: May 25, 2023

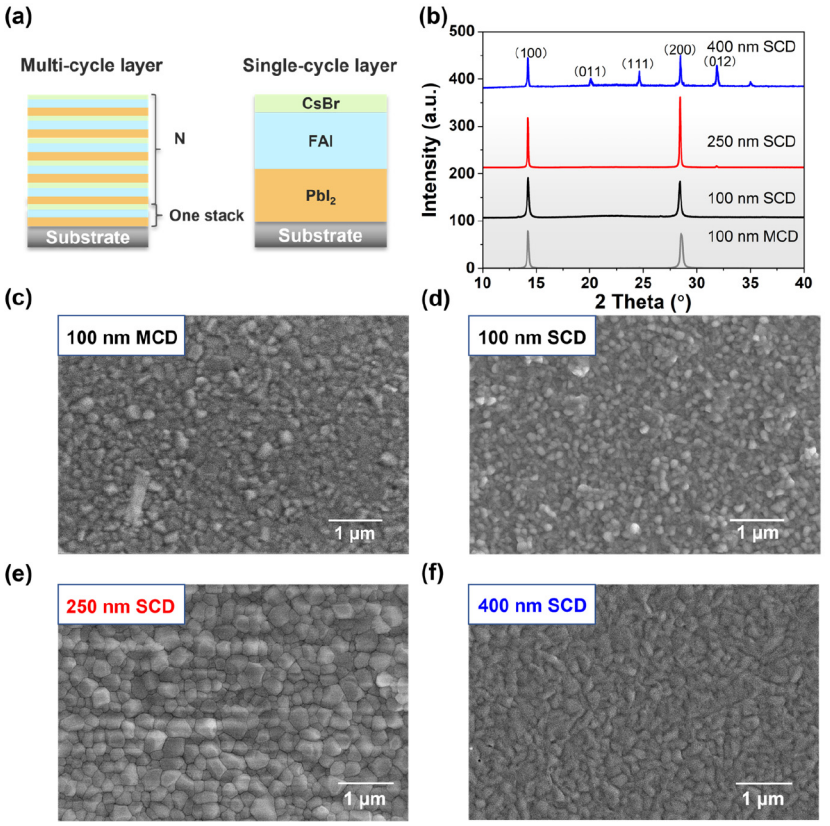

Figure 1. (a) Schematic illustration of the preparation procedure of PVK films by MCD and SCD. (b) XRD patterns of the MCD precursor film (gray) and SCD films. (c–f) Top-view SEM images of samples reported in panel (b) with different thicknesses. All the films are annealed at 100 °C for 30 min.

deposition studies based on three or more precursors have been reported.[10]

In using sequential thermal evaporation, individual layers of the precursors are deposited. This can be done in a multicycle approach yielding an array of precursor layers or in a single-cycle approach yielding thick films of each individual precursor (see Figure 1a). Although the latter is a straightforward and cost-effective method, in particular, the nonuniform elemental distribution across the film might lead to local non-stoichiometry.[9] A postannealing treatment is yet expected to enhance the interdiffusion and improve the element distribution. However, as mentioned above, little information regarding this method of deposition is available. Therefore, it is meaningful to investigate the optoelectronic properties of PVK films prepared from precursors varying in thickness, during and after the postdeposition annealing.

The mixed-cation, mixed-halide PVK $Cs_xFA_{1-x}PbI_{3-x}Br_x$ exhibits good thermal and phase stability.[13] In this work, we propose to use the single-cycle deposition (SCD) procedure to prepare high-quality and uniform CsFAPbIBr PVK films. The impact of PVK thickness as well as annealing is systematically investigated in terms of crystallinity, in-depth uniformity, and optoelectronic properties. Also, the conversion from precursors to PVK during postdeposition annealing is also studied in detail with grazing incidence X-ray diffraction (GI-XRD). We find that, by applying an optimized annealing treatment, CsFAPbIBr deposited with SCD shows comparable optoelectronic properties to the one deposited by multicycle deposition (MCD). Moreover, we found that cesium bromide (CsBr) accelerates the interdiffusion of formamidinium iodide (FAI) over the different layers, supporting the crystallization of PVK. With this straightforward approach, the 250 nm SCD PVK film's half-intensity lifetime ($\tau_{1/2}$) reaches around 650 ns with carrier mobility close to 10 $cm^2\ V^{-1}\ s^{-1}$. This work demonstrates that precursors can be deposited by SCD and that relatively thick precursor layers can still react to fully convert into PVK through the film. The understanding of the influence of the postdeposition annealing treatment on the precursor diffusion and on the reaction mechanism provides directions for further improving the thermally evaporated PVK deposition.

EXPERIMENTAL DETAILS

Material and Film Preparation. $CH(NH_2)_2I$ (FAI) (99.9%), CsBr, and PbI_2 (99.999%) were purchased from Sigma-Aldrich and used as received. Quartz and Corning glass substrates were cleaned according to a standard procedure consisting of acetone, ethanol, and an ozone treatment for 5 min. After cleaning, the substrates were directly transferred into a N_2-filled glovebox and loaded into the deposition chamber (AJA). The chamber was evacuated reaching a base pressure of 5×10^{-6} mbar before the sources were heated. During film preparation, precursors were sequentially deposited forming one stack. The deposition order was PbI_2, FAI, and CsBr for $Cs_xFA_{1-x}PbI_{3-x}Br_x$, while it was PbI_2, FAI for $FAPbI_3$. The target thickness was obtained by repeating the stack number (N), where N = 20 for MCD and N = 1 for SCD. The PbI_2 was evaporated at the temperature of ~240 °C, and the corresponding deposition rate was stabilized at 0.4–0.5 Å/s. FAI was evaporated on top of the as-deposited PbI_2 film, and the evaporation rate of FAI reached 0.3–0.4 $Å/s^{-1}$ with the crucible temperature of ~100 °C. As for CsBr, the source was evaporated with a rate of 0.08–0.10 Å/s at ~380 °C. Evaporation rates and film thicknesses were monitored by one quartz

https://doi.org/10.1021/acsaem.3c00203
ACS Appl. Energy Mater. XXXX, XXX, XXX–XXX

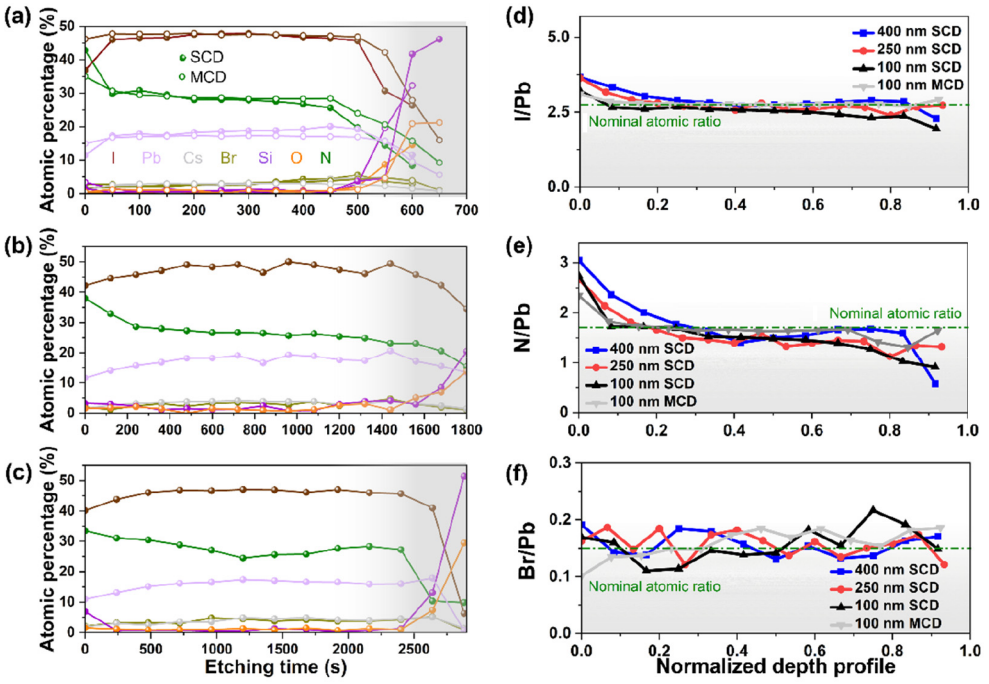

Figure 2. XPS depth atomic percentage profile of PVK films with different thicknesses: (a) 100 nm MCD layer (open symbols) and SCD samples (full symbols), (b) 250 nm SCD sample, (c) 400 nm SCD sample. (d–f) Corresponding XPS depth atomic ratios of PVK films with different thicknesses for (d) I/Pb, (e) N/Pb, and (f) Br/Pb. The green dashed line indicates the nominal ratio.

crystal microbalance. Taking into consideration different tooling factors, the target PVK film thicknesses were set to reach 100, 250, and 400 nm by adapting the N or thickness of each precursor layer in one stack (shown in Table S1). The detailed processing information (such as evaporating temperature, chamber pressure, and deposition rates) is shown in Table S2. The as-deposited PVKs were then annealed under 100 °C for 30 min in the glovebox before characterization.

Characterization. XRD patterns were measured with a Bruker D8 Advance diffractometer equipped with a Cu–Kα X-ray source that has a wavelength of 1.54 Å. Grazing incident XRD (GIXRD, Bruker D8 Discover, Cu Kα) was performed with incident angles of 0.25, 0.5, 1, 3, and 5° to vary the information depth. The measurements were carried out in vacuum at 10^{-4} mbar inside an Anton Paar XRK900 Reactor Chamber equipped with Be windows. On the primary side, a Goebel mirror was used together with a fixed slit of 0.1, 0.1, 0.2, 0.6, and 1.0 mm, respectively, for the incident angles to control the footprint on the film. On the secondary side, a Soller 2.5° slit was used, and the LYNXEYE XE detector was operated in 0D high-resolution mode.

The elemental composition of the PVK films was analyzed by X-ray photoelectron spectroscopy using a ThermoScientific K-Alpha spectrometer. The spectrometer is equipped with a focused monochromatic Al–Kα X-ray source (1486.6 eV) operating at 36 W (12 kV, 3 mA). The spot-size is approximately 800 × 400 μm^2. The pass energy of the analyzer was set to 50 eV. A flood gun was operated at 1 V, 100 μA to prevent charging of the sample. The base pressure in the analysis chamber was approximately 2 × 10^{-9} mbar. Three points are measured for one sample to take an average.

Depth profiling was performed by etching the sample with argon ions. The voltage of the ion gun was set to 1000 eV for in-depth etching for both 100 and 250 nm thick samples, while a higher voltage of 2000 eV was applied to the 400 nm thick sample, due to protection of the XPS machine with shortened etching time. Detailed analysis was performed with the Avantage software, where 70% Gaussian and 30% Lorentzian line shapes (weighted least-squares fitting method) and a nonlinear Shirley-type background were used to fit the peaks. Atomic percentages were calculated based on the fitted peak areas and the corresponding sensitivity factors of the detailed scans. The binding energy was corrected for the charge shift by taking the done relative to the primary C 1s hydrocarbon peak at BE = 284.8 eV as a reference.

The surface morphology of the PVK films were measured by the scanning electron microscope (SEM, JEOL) under an accelerating voltage of 8 keV.

The absorptance spectra of samples were measured by ultraviolet–visible spectroscopy (UV/vis, PerkinElmer, Lambda 1050) within a wavelength range of 300–800 nm.

The photoluminescence spectra of the samples were investigated by the steady-state photoluminescence setup (PL, FLS 980) with an excitation wavelength of 420 nm, while the emission light was filtered by a 550 nm filter. The time-resolved photoluminescence was measured with the setup (Lifespec) with an excitation wavelength of 405 nm. The detailed measurement was described in ref 14.

Time-resolved microwave conductance (TRMC) was applied to learn about the carrier lifetime, mobility, and trap densities. All the measurement parameters can be found in ref 15.

RESULTS AND DISCUSSION

Figure 1a shows the schematic cross sections of the PVK film preparation process based on MCD and SCD thermal evaporation to produce CsFAPbIBr.

Thickness Effects on SCD Layers. To learn about the thickness-related PVK film properties, we measured crystal structure, in-depth uniformity, and optoelectronic properties of samples with different target thicknesses (100, 250, and 400 nm). Figure 1b shows the XRD patterns of the 100 nm thick CsFAPbIBr reference layer obtained with MCD and three CsFAPbIBr films obtained using SCD with thicknesses from 100 to 400 nm. For the MCD layer, we observe the presence of two main peaks at 2θ = 14.08° and 2θ = 28.32° corresponding to the (100) and (200) planes of the PVK. As no other intense reflections are present, this indicates a preferable crystal growth.[16] Both the 100 and 250 nm thick SCD films share a similar pattern with the reference film, and the detailed peak information is provided in Table S3. The presence of two main

https://doi.org/10.1021/acsaem.3c00203
ACS Appl. Energy Mater. XXXX, XXX, XXX–XXX

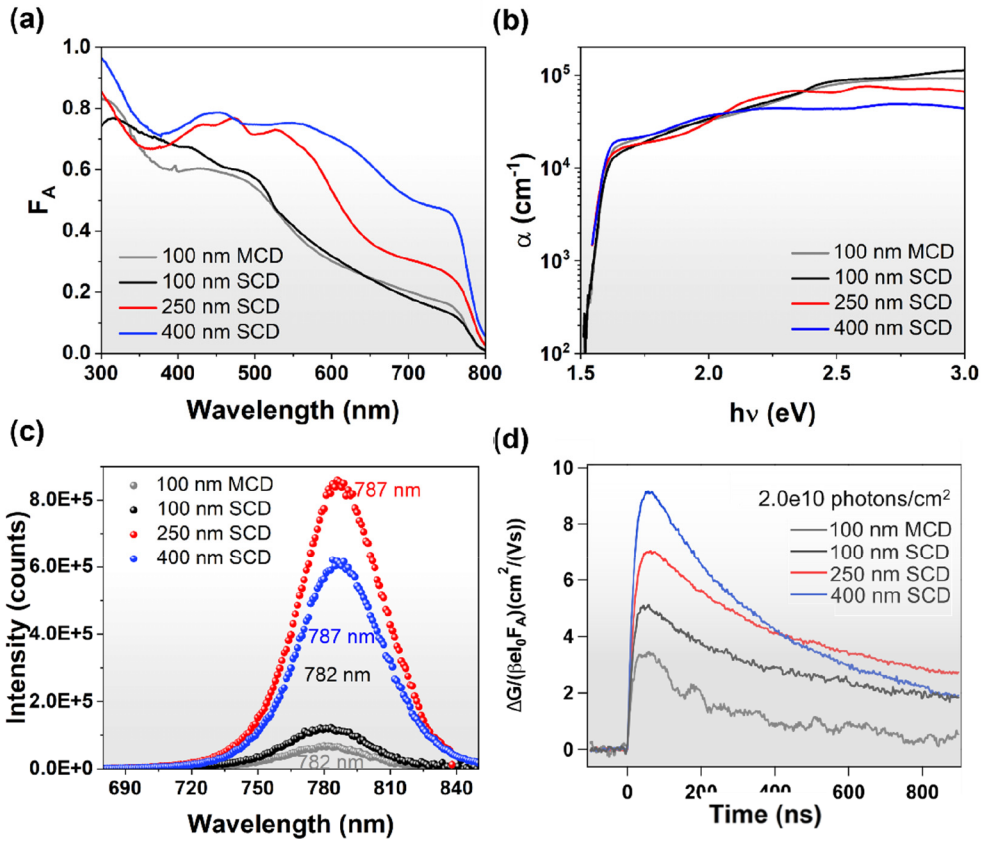

Figure 3. Optical and opto-electronic properties of 100 nm MCD and SCD layers with different thicknesses. (a) Fraction of light absorbed (F_A), (b) semilogarithmic plot of the absorption coefficients, (c) steady-state PL, and (d) TRMC measurement with photon intensity of 2e10 cm^2 per pulse.

peaks in both the 100 and 250 nm thick SCD PVK films highlights the preferential orientation of the grains.[12] Interestingly, this kind of orientation disappears as the thickness increases to 400 nm for the SCD sample.[17] When we focus on the (100) peak of the samples with different thicknesses (Figure S1 and Table S3), we notice no shift in peak position, which is consistent with a constant I/Br ratio across the film thickness.[18]

To investigate the film morphology as a function of the thicknesses and deposition process, we report SEM top-view images in Figure 1c–f. Looking at the two 100 nm thick samples, the SCD layer shows an average grain size of ∼100 nm, which is slightly smaller than the reference MCD layer, which is around ∼130 nm. The corresponding grain size statistics are shown in Figure S2. The decreased grain size for the SCD film could be attributed to the increased number of nucleation sites during deposition.[19] Note that in the single-cycle approach, PbI_2 forms the substrate on which the FAI layer is deposited, as shown in Figure 1a. Differently, the mixed precursor/PVK already formed in MCD, which is shown as the template layer for the subsequent stack. Furthermore, we observed in Figures 1c–f (and Figure S2) that the grain size gradually increases as the film thickness increases from 100 to 250 nm, while the grain shapes show a small change. The increased grain size mainly comes from improved crystallinity.[20] Differently, the grain shape is observed elongated in the horizontal direction for the 400 nm thick sample, which originates from the changing of crystal orientation growth, resulting from the degree of precursor reaction.[21]

Furthermore, we studied the role of annealing time on the crystal growth by looking at the evolution of film's microstructure for various annealing times (30 s, 1 min, and 30 min) by SEM inspection as shown in Figure S3. For the 250 nm thick sample, there is no apparent grain shape change, while the grain size shows a slight increase from a 30 s to 30 min annealing time, in agreement with the XRD results in Figure S4a calculated from Scherrer equation.[22] Differently, the 400 nm thick sample shows an apparent grain shape change from 30 s to 1 min, which comes from the formation of non-orientation-preferred PVK polycrystalline.

To examine the chemical composition across the film, we measured samples with different thicknesses by XPS after specific periods of etching as shown in Figure 2. The atomic percentages and element ratios through the film are plotted as a function of the etching time. The XPS high-resolution spectra of Pb $4f_{7/2}$, C 1s, N 1s, Cs $3d_{5/2}$, I $3d_{5/2}$, and Br 3d can be found in Figure S5 for the 100 nm thick SCD sample as an example to show the fitting and extraction of raw data. The averaged atomic percentage of different elements for all samples extracted from Figure 2 are summarized in Table S4. In Figure 2a, we note that both MCD and SCD layers with a thickness of 100 nm show similar atomic percentage trends for N, Cs, Br, Pb, and I, indicating comparable element depth-dependent uniformity irrespective of the preparation procedure used. With increased film thickness, we observe an almost stable composition along the film for the 250 nm thick sample (Figure 2b), while the 400 nm thick one exhibits atomic percentage variation, as shown in Figure 2c. In particular, the

https://doi.org/10.1021/acsaem.3c00203
ACS Appl. Energy Mater. XXXX, XXX, XXX−XXX

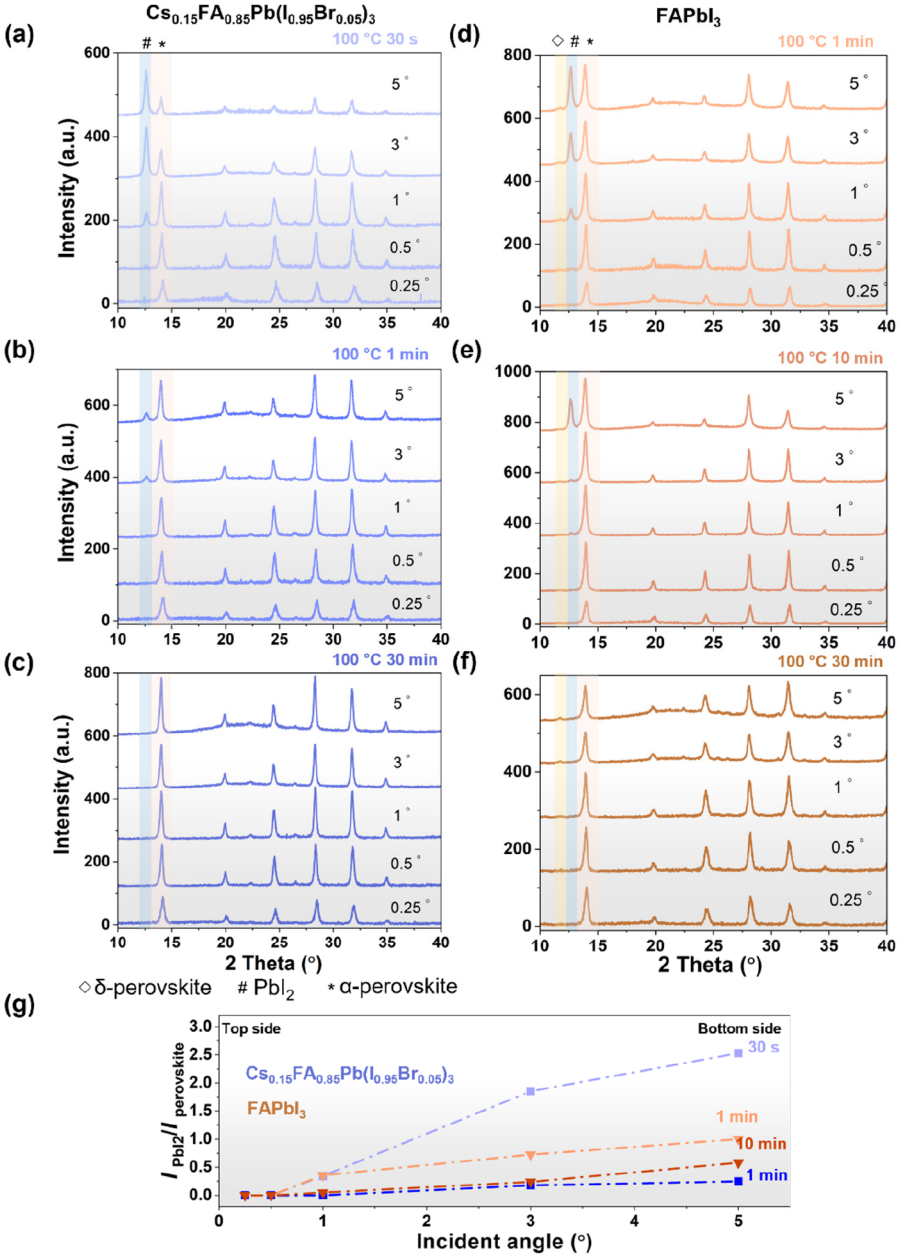

Figure 4. (a–c) GIXRD measurements on 400 nm thick CsFAPbIBr films with different annealing times: (a) 30 s, (b) 1 min, and (c) 30 min. (d–f) GIXRD measurements on 400 nm thick $FAPbI_3$ with different annealing times: (d) 1 min, (e) 10 min, and (f) 30 min. The δ-phase PVK peak is highlighted in yellow; the PbI_2 (100) peak is highlighted in light blue; and the PVK (100) peak is highlighted in light brown. (g) Dependence of the I_{PbI2}/I_{PVK} (100) ratio extracted from Figure 4(a–f) as a function of incident angle for CsFAPbIBr and $FAPbI_3$ at different annealing times.

N (Pb) atomic percentage shows a clear drop (increase) for etching times longer than 1200 s. This phenomenon may suggest that for the thicker layer, FAI is unable to uniformly diffuse under 100 °C and a 30 min annealing due to the thicker layer. Therefore, a longer annealing time is applied to the film, and the corresponding XRD patterns are shown in Figure S6. Clearly, the samples with 45 and 60 min of annealing indicate the appearance of the PbI_2 peak compared with the ones with shorter annealing times, showing some thermal degradation. Thus, the SCD 400 nm thick PVK film exhibits a problem with the balance between FAI uniform distribution and thermal degradation during annealing optimization. To compare the in-depth precursor ratios, we report in Figure 2d–f, the calculated atomic ratios I/Pb, N/Pb, and Br/Pb as a function of the normalized in-depth profile. The N/Pb gives an indication of the FAI distribution along the film thickness, and the Br/Pb ratio is related to the bandgap variation. The nominal atomic ratio for I/Pb (N/Pb, Br/Pb) is equal to 2.85 (1.7 and 0.15) in the CsFAPbIBr PVK structure, and it is shown as dashed lines in Figure 2d–f. The I/Pb ratio shows similar trends for 100 nm SCD samples compared with the 100 nm thick MCD sample, while the 400 nm thick SCD sample exhibits a high I/Pb ratio and slow I/Pb drop at the top of the film compared with the ratio of the 100 nm thick samples (Figure 2d). Similarly, an initial high FA is observed for a 400 nm thick SCD sample in Figure 2e, which further indicates a nonuniform distribution of FAI. Different trends are found for Br/Pb in Figure 2f, proving different diffusion lengths of FAI and CsBr precursors in PbI_2,

https://doi.org/10.1021/acsaem.3c00203
ACS Appl. Energy Mater. XXXX, XXX, XXX−XXX

which can be explained as the FAI molecular size being larger compared with CsBr.[23]

As annealing drives molecular diffusion, we characterized the 400 nm thick samples by XPS before annealing to evaluate the impact of the annealing treatment on the elemental distribution (Figure S7). In the as-deposited 400 nm thick sample, we observed noticeable distribution variations with a gradual drop of the N/Pb (from ∼2 to ∼0.2) calculated by the atomic profile as etching goes from the PVK surface toward the PVK/quartz interface. In addition, the I/Pb ratio at the bottom of the film is equal to 2, showing that FAI can hardly penetrate through the bottom of the film. These results indicate the hampering of the FAI diffusion into the PbI_2 during deposition (without annealing). On the contrary, both Br and Cs are detected across the entire PVK film thickness even though the Br/Pb ratio gradually decreases when approaching the PVK/quartz interface. This finding further confirms the longer diffusion length of CsBr in PbI_2 compared to FAI.

In addition to the crystal structure, morphology, and uniformity, we carried out more investigations to probe the optoelectrical properties of CsFAPbIBr films fabricated via SCD. Figure 3a,b shows different optical properties with varying film thicknesses. Specifically, the spectra in Figure 3a of the PVKs show improved absorptance at the long wavelength range due to increased thickness. The absorption coefficients (α) are compared in Figure 3b. The absorption coefficient of 100 nm thick SCD samples overlaps well with the one of the 100 nm thick MCD sample. All the films show an α at the level of 10^4 cm^{-1}. Also, all these samples present a sharp absorption edge corresponding to a bandgap of ∼1.58 eV as determined by the Tauc plot of Figure S8a. These values are in agreement with published work on PVKs having a similar composition.[24]

To investigate the thickness-related film optoelectrical properties, carrier lifetime, mobility, and trap densities are determined by applying steady-state PL, TRPL, and TRMC. Figure 3c reports the steady-state PL spectra of all samples. The spectra are symmetric and can be well-fitted by a single Gaussian peak. In addition, the peak positions show a slight red shift from 782 nm (1.58 eV) to 787 nm (1.57 eV) as the film thickness increases. This kind of peak shift is related to the variation of precursor composition, as indicated by the increased *d*-value in Table S3. Furthermore, the I/Br calculated from the averaged atomic percentage shown in Table S4 further verified the composition effects on the film optoelectrical properties. The dynamics of the charge carrier recombination are analyzed by TRPL as shown in Figure S8b. Interestingly, the 250 nm thick sample shows an even longer lifetime compared to the 400 nm thick sample, benefiting from its better crystal orientation.[25]

In contrast to TRPL, TRMC gives information regarding the free charge carrier mobility and lifetime (Figure 3d). In view of the low exciton binding energy of CsFA-based PVK, we can assume that the free charge carrier generation yield, φ, is close to unity at room temperature. Therefore, we conclude that the sum of the effective electron and hole mobilities, $\Sigma\mu$, increases from 5 to 9 cm^2 V^{-1} s^{-1} with increasing the film thickness. This improvement can be explained by the increased crystal size, verified by the SEM results in Figure 1c−f.[26] Nevertheless, the lifetime of 400 nm thick film is shorter than the 250 nm one, which is in accordance with the TRPL. One reason is that the orientation growth of 250 nm film can suppress trap recombination. The other reason is that the TRMC measures all free carriers both at the surface and in the bulk. Compared to the TRPL results, TRMC verified that the 400 nm thick PVK film needs further annealing treatment to improve the crystallization. Moreover, the TRMC with various incident light intensities is shown in Figure S9 based on samples with different thicknesses. It should be noted that both the 250 and 400 nm thick samples exhibit comparable carrier mobility and lifetime to other published works, which are based on thermal coevaporation methods;[9,27] the detailed data are summarized in Table S6. Therefore, we conclude that the variation of thickness in SCD affects the film optoelectronic properties performance because of the precursor diffusion, reaction (Figure 2), and crystal growth (Figure 1).

Crystallization of the Single-Cycle Thermally Evaporated PVK during Annealing. The results discussed above indicate that the SCD process can reach comparable film properties with MCD for 100 nm thick film, and it can be expanded to thicker layers up to 250 nm. However, the precursor diffusion and reaction process during annealing is still not fully understood. Therefore, it is meaningful to study the conversion of PVK during annealing. To this end, 400 nm thick samples subjected to annealing times ranging from 30 s to 30 min are monitored by GIXRD. By increasing the incident angle stepwise from 0.25 to 5°, we increase the information depth of the XRD measurement to obtain depth-dependent structural information regarding the PVK and PbI_2 phases. The GIXRD patterns of a 400 nm thick CsFAPbIBr film shown in Figure 4a−c exhibit five main peaks at 2θ of 14.2, 20.0, 24.6, 28.4, and 31.8°, which can be assigned to the (100), (011), (111), (200), and (012) planes of cubic PVK.[12] The additional two diffraction peaks at 11.8 and 12.7° correspond to the δ-phase PVK and the (100) peak of PbI_2, respectively.[28] Even at only 30 s of annealing at 100 °C, the appearance of the PVK peaks in Figure 4a shows that a substantial amount of the precursors has already converted into PVK, although unreacted PbI_2 is still visible, in particular at large incident angles. These results show that the top region has fully converted into PVK, while the bottom part exhibits a mixture of PbI_2 and PVK. With a longer annealing period of 1 min, a weak PbI_2 peak is only observed at large incident angles, indicating the presence of unreacted precursor in the bottom of the PVK layer, as shown in Figure 4b. After 30 min of annealing, no PbI_2 peak is detected at any incident angle (Figure 4c), showing that PbI_2 has completely converted into PVK.

To further understand the crystallization process as well as the role of CsBr in the conversion during annealing, 400 nm thick $FAPbI_3$ layers are prepared by SCD. The samples are annealed at 100 °C for 30 s, 1 min, 10 min, 30 min and measured by GIXRD. The $FAPbI_3$ sample annealed for 30 s resulted to be particularly unstable during the sample transfer, which comes from the conversion from $FAPbI_3$ PVK into yellow phase.[29] Thus, this result is not included in Figure 4. The $FAPbI_3$ film annealed for 1 min shown in Figure 4d exhibits a high relative intensity of PbI_2/PVK (100) at incident angles of both 3 and 5°, while no peak is spotted at lower incident angles, indicating relatively large amounts of unreacted PbI_2 at the bottom of film. Furthermore, even after 10 min of annealing, the PbI_2 peak is still visible at 5°, as shown in Figure 4e, indicating there is still some unreacted PbI_2 at the bottom. Only for the longest annealing time of 30 min is no PbI_2 peak detected (Figure 4f). From this comparison, we can conclude that the presence of CsBr accelerates the precursor conversion into PVKs. The fact that after 10 min of postannealing thermal treatment, there is still

https://doi.org/10.1021/acsaem.3c00203
ACS Appl. Energy Mater. XXXX, XXX, XXX−XXX

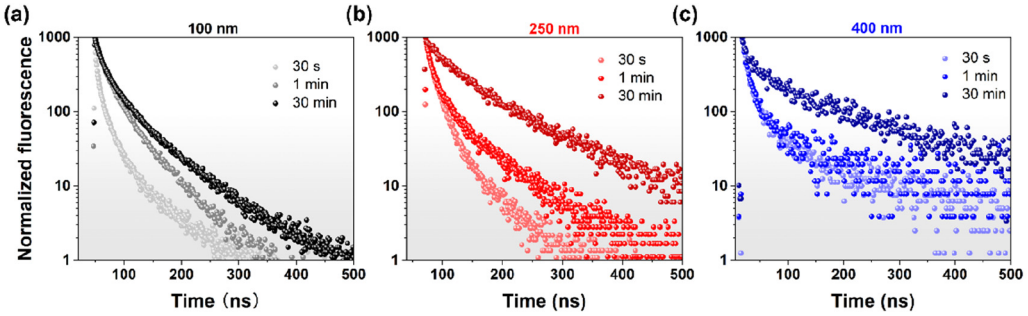

Figure 5. Evolution of optoelectrical properties of SCD $Cs_xFA_{1-x}PbI_{3-x}Br_x$ annealed at 100 °C and variable time. (a–c) TRPL of 100, 250, and 400 nm SCD samples annealed at 30 s, 1 min, and 30 min.

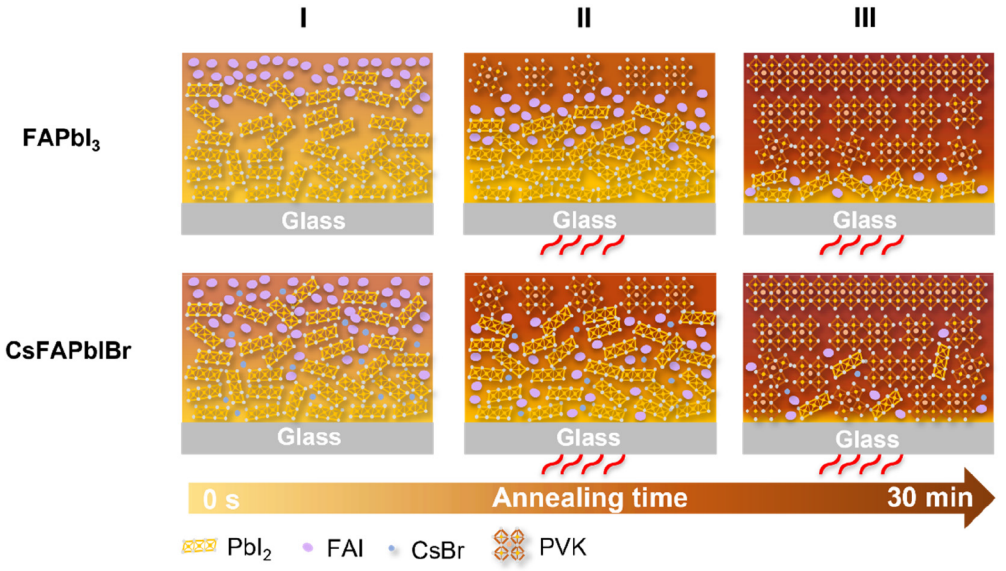

Figure 6. Schematic of the PVK conversion process for both CsFAPbIBr and $FAPbI_3$ during annealing.

PbI_2 at the bottom of the $FAPbI_3$ film suggests that, in the absence of CsBr, mixing of the precursors limits the complete PVK conversion.

To further classify the CsBr induced difference between CsFAPbIBr and $FAPbI_3$ during annealing, the I_{PbI2}/I_{PVK} ratios from Figure 4a–f are plotted as a function of the incident angle for both CsFAPbIBr and $FAPbI_3$ to visualize the in-depth reaction process as shown in Figure 4g. The I_{PbI2}/I_{PVK} ratios increase going deeper into the film for both PVK materials investigated and all annealing times, but their slopes are very different from each other's. The steep slope change for CsFAPbIBr from 30 s annealing to 1 min annealing in Figure 4g visually indicates that the presence of CsBr assists precursor mixing and accelerates PVK conversion during annealing. We note that in general interpreting GIXRD measurements of samples with preferred orientation is difficult and should be taken with the necessary precautions, as both depth-dependence and preferred orientation can cause a variation of the (relative) peak intensity with incident angle. Although the preferential orientation of the PbI_2 phase complicates also here the interpretation, we believe that the consistent trends among the different samples with different annealing times and in particular the different ratios of I_{PbI2}/I_{PVK} of the different samples strongly indicate that the variations of the PbI_2 peak intensity also reflect a depth-dependence of the PbI_2 concentration. Apart from the PVK crystal formation, the evolution of film optoelectronic properties upon annealing is also analyzed. We measure TRPL on 100, 250, and 400 nm thick SCD samples with different annealing times (30 s, 1 min, and 30 min), as shown in Figure 5a–c. All these samples show annealing time-dependent PL decay, and the lifetime is extended by longer annealing time due to higher crystallinity. For the 100 nm sample, the initial part of the TRPL signal of the 1 min overlays with the one of 30 min annealing. In contrast, for the 400 nm thick sample, the initial part of the TRPL signal of the 1 min overlays with the 30 s annealed signal. For the 250 nm thick sample, an intermediate behavior is found.

From the above, for the 400 nm thick sample, a 30 min annealing time is required to obtain long TRPL lifetimes, even though from structural (Figure S6) and optical (Figure S11) measurements, the PVK conversion seems to be complete even after only 1 min of annealing. In contrast, for the 100 nm thick sample, 1 min of thermal treatment seems sufficient to reach optimal optoelectronic properties. It indicates that the structural and optical properties are asynchronous with electrical properties during annealing, and this phenomenon is strongly dependent on film thickness.

As confirmed by GIXRD, the precursors exhibit a reaction-limited process during annealing. To look further into this process, we measured the optoelectronic properties of the 400 nm thick CsFAPbIBr with different annealing times in Figures

https://doi.org/10.1021/acsaem.3c00203
ACS Appl. Energy Mater. XXXX, XXX, XXX–XXX

S11 and S12. The PVK conversion can also be examined by measuring the evolution of optoelectronic properties during annealing. The PVK absorption onset starts to form after 30 s of annealing, and a continuous increase of the absorptance was observed from 300 to 800 nm for longer annealing times. In contrast to the 400 nm thick sample, the 250 nm thick samples show a similar absorptance for 1 and 30 min annealing (Figure S4b), especially at longer wavelengths. This implies that the conversion into PVK has already finished, in line with the XRD results shown in Figure S4a. PL spectra were also recorded as a function of the annealing time by illuminating through the quartz substrate (back) and PVK surface (front) of the 400 nm thick SCD sample as shown in Figure S12. The peak shape and position are altered by illuminating from different sides for both 30 s and 1 min annealed samples, suggesting that there are compositional changes through the cross section of the film.

Role of CsBr in PVK Conversion in SCD Films during Postdeposition Annealing. Combining the information obtained by GIXRD, XPS, UV−vis, and PL measurements during the annealing of the SCD film, we propose the following mechanism for the formation of CsFAPbIBr. Three stages take place during the entire process as depicted in Figure 6 for both CsFAPbIBr and $FAPbI_3$.

In the as-deposited film (stage I in Figure 6), FAI and PbI_2 almost keep as individual stacks for $FAPbI_3$ film, while FAI shows concentration driving gradient distribution in PbI_2 film for CsFAPbIBr, as indicated in the XPS profile in Figure S7. Furthermore, signals of both Cs and Br were detected through the film and even at the bottom of the as-deposited CsFAPbIBr layer (Figure S7). As annealing time goes on, precursors partially convert into PVKs through the film for both CsFAPbIBr and $FAPbI_3$, as shown in stage II in Figure 6. Compared with $FAPbI_3$, the existence of CsBr assists the precursor mixing and leads to the fast formation of CsFAPbIBr, which only takes a few minutes to realize a full conversion of PVK through the film (Figure 4). We attribute this difference to the role of CsBr that is already uniformly distributed through the film (Figure S7). As for stage III at the end of annealing, unreacted precursors are detected at the bottom of the $FAPbI_3$ film, while unreacted PbI_2 exists through the CsFAPbIBr film because of the different precursor mixing levels.

CONCLUSIONS

We demonstrated a simple sequential evaporation technique to prepare high-quality PVK films based on multisource deposition. By sequentially depositing the precursors into a single stack, highly crystalline $Cs_{0.15}FA_{0.85}PbI_{2.85}Br_{0.15}$ is obtained after optimized annealing treatment. This single-cycle deposition film shows thickness-dependent optoelectronic properties. As the target thickness increases to 400 nm, the film shows a drop in optoelectronic properties even though it structurally shows a PVK diffraction peak with optimized annealing. This phenomenon might be explained by the limited diffusion length of these precursors in single-cycle deposited 400 nm thick PVK film. To improve the composition uniformity for thick samples, further strategies could be explored: (1) Change the deposition order; (2) first layer morphology optimization (annealing or atmosphere treatment); (3) introducing small-sized cations and halides in as-deposited films. We also studied the precursor reaction during postdeposition annealing, the crystal structure, and optoelectronic properties as a function of different annealing times. The structural and optical properties are asynchronous with electrical properties during annealing, which is strongly dependent on film thickness, resulting from precursor mixing and reacting. In addition, the presence of CsBr can assist the precursor mixing during annealing, which is beneficial to the fast precursor reaction and PVK conversion. The strategy used in this work provides an alternative way for uniform and large-scale vacuum deposition for PVK-based photovoltaic technology.

ASSOCIATED CONTENT

Supporting Information

The Supporting Information is available free of charge at https://pubs.acs.org/doi/10.1021/acsaem.3c00203.

Grain size distribution, tilted and top-view SEM images, XPS raw data and in-depth element distribution, thickness-dependent optical absorption, Tauc plot, photoluminescence and time-resolved photoluminescence results, detailed TRMC results, table with thicknesses of deposited stacks and details of annealing treatment, a table with processing conditions for thermal evaporation (temperature, deposition rate, and vacuum), a table with XPS details for each peak, and tables with fitting parameters extracted from TRPL (PDF)

AUTHOR INFORMATION

Corresponding Authors

Tom J. Savenije − *Department of ChemE, Delft University of Technology, 2629 HZ Delft, The Netherlands;* orcid.org/0000-0003-1435-9885; Email: T.J.Savenije@tudelft.nl

Luana Mazzarella − *PVMD group, Delft University of Technology, 2628 CD Delft, The Netherlands;* Email: L.Mazzarella@tudelft.nl

Authors

Jin Yan − *PVMD group, Delft University of Technology, 2628 CD Delft, The Netherlands; Department of ChemE, Delft University of Technology, 2629 HZ Delft, The Netherlands*

Jiashang Zhao − *Department of ChemE, Delft University of Technology, 2629 HZ Delft, The Netherlands*

Haoxu Wang − *PVMD group, Delft University of Technology, 2628 CD Delft, The Netherlands;* orcid.org/0000-0002-5430-0899

Mels Kerklaan − *PVMD group, Delft University of Technology, 2628 CD Delft, The Netherlands; Department of ChemE, Delft University of Technology, 2629 HZ Delft, The Netherlands*

Lars J. Bannenberg − *Faculty of Applied Sciences, Delft University of Technology, 2629 JB Delft, The Netherlands;* orcid.org/0000-0001-8150-3694

Bahiya Ibrahim − *Department of ChemE, Delft University of Technology, 2629 HZ Delft, The Netherlands*

Olindo Isabella − *PVMD group, Delft University of Technology, 2628 CD Delft, The Netherlands*

Complete contact information is available at: https://pubs.acs.org/10.1021/acsaem.3c00203

Notes

The authors declare no competing financial interest.

https://doi.org/10.1021/acsaem.3c00203
ACS Appl. Energy Mater. XXXX, XXX, XXX−XXX

■ ACKNOWLEDGMENTS

The authors would like to thank Bart Boshuizen (Faculty of Applied Sciences, Delft University of Technology) for support in XPS measurement and Xiaohui Liu (Faculty of Applied Sciences, Delft University of Technology) for support in XRD measurement.

■ REFERENCES

(1) Wang, Y.; Zhang, Y.; Zhang, P.; Zhang, W. High intrinsic carrier mobility and photon absorption in the perovskite $CH_3NH_3PbI_3$. *Phys. Chem. Chem. Phys.* **2015**, *17* (17), 11516−11520.

(2) Bai, S.; Wu, Z.; Wu, X.; Jin, Y.; Zhao, N.; Chen, Z.; Mei, Q.; Wang, X.; Ye, Z.; Song, T.; Liu, R.; Lee, S.; Sun, B. High-performance planar heterojunction perovskite solar cells: Preserving long charge carrier diffusion lengths and interfacial engineering. *Nano Research* **2014**, *7* (12), 1749−1758.

(3) Steirer, K. X.; Schulz, P.; Teeter, G.; Stevanovic, V.; Yang, M.; Zhu, K.; Berry, J. J. Defect Tolerance in Methylammonium Lead Triiodide Perovskite. *ACS Energy Letters* **2016**, *1* (2), 360−366.

(4) Min, H.; Lee, D. Y.; Kim, J.; Kim, G.; Lee, K. S.; Kim, J.; Paik, M. J.; Kim, Y. K.; Kim, K. S.; Kim, M. G.; Tae, J. S.; Sang, S.; et al. Perovskite solar cells with atomically coherent interlayers on SnO2 electrodes. *Nature* **2021**, *598* (7881), 444−450.

(5) Xu, F.; Zhang, T.; Li, G.; Zhao, Y. Mixed cation hybrid lead halide perovskites with enhanced performance and stability. *Journal of Materials Chemistry A* **2017**, *5* (23), 11450−11461.

(6) Yan, J.; Savenije, T. J.; Mazzarella, L.; Isabella, O. Progress and challenges on scaling up of perovskite solar cell technology. *Sustainable Energy & Fuels* **2022**, *6* (2), 243−266.

(7) Kim, B. S.; Gil-Escrig, L.; Sessolo, M.; Bolink, H. J. Deposition Kinetics and Compositional Control of Vacuum-Processed $CH_3NH_3PbI_3$ Perovskite. *J. Phys. Chem. Lett.* **2020**, *11* (16), 6852−6859.

(8) Kim, B. S.; Han, Y.; Kim, J. J. Growth mechanism of CH_3NH_3I in a vacuum processed perovskite. *Nanoscale Adv.* **2020**, *2* (9), 3906−3911.

(9) Li, J.; Dewi, H. A.; Wang, H.; Zhao, J.; Tiwari, N.; Yantara, N.; Malinauskas, T.; Getautis, V.; Savenije, T. J.; Mathews, N.; Mhaisalkar, S.; Bruno, A. Co-Evaporated MAPbI3 with Graded Fermi Levels Enables Highly Performing, Scalable, and Flexible p-i-n Perovskite Solar Cells. *Adv. Funct. Mater.* **2021**, *31* (42), 2103252.

(10) Feng, J.; Jiao, Y.; Wang, H.; Zhu, X.; Sun, Y.; Du, M.; Cao, Y.; Yang, D.; Liu, S. High-throughput large-area vacuum deposition for high-performance formamidine-based perovskite solar cells. *Energy Environ. Sci.* **2021**, *14* (5), 3035−3043.

(11) Gil-Escrig, L.; Dreessen, C.; Palazon, F.; Hawash, Z.; Moons, E.; Albrecht, S.; Sessolo, M.; Bolink, H. J. Efficient Wide-Bandgap Mixed-Cation and Mixed-Halide Perovskite Solar Cells by Vacuum Deposition. *ACS Energy Lett.* **2021**, *6* (2), 827−836.

(12) Ji, R.; Zhang, Z.; Cho, C.; An, Q.; Paulus, F.; Kroll, M.; Löffler, M.; Nehm, F.; Rellinghaus, B.; Leo, K.; Vaynzof, Y. Thermally evaporated methylammonium-free perovskite solar cells. *Journal of Materials Chemistry C* **2020**, *8* (23), 7725−7733.

(13) Tan, W.; Bowring, A. R.; Meng, A. C.; McGehee, M. D.; McIntyre, P. C. Thermal Stability of Mixed Cation Metal Halide Perovskites in Air. *ACS Appl. Mater. Interfaces* **2018**, *10* (6), 5485−5491.

(14) Zhao, J.; Caselli, V. M.; Bus, M.; Boshuizen, B.; Savenije, T. J. How Deep Hole Traps Affect the Charge Dynamics and Collection in Bare and Bilayers of Methylammonium Lead Bromide. *ACS Appl. Mater. Interfaces* **2021**, *13* (14), 16309−16316.

(15) Hutter, E. M.; Gelvez-Rueda, M. C.; Osherov, A.; Bulovic, V.; Grozema, F. C.; Stranks, S. D.; Savenije, T. J. Direct-indirect character of the bandgap in methylammonium lead iodide perovskite. *Nat. Mater.* **2017**, *16* (1), 115−120.

(16) Ng, A.; Ren, Z.; Shen, Q.; Cheung, S. H.; Gokkaya, H. C.; Bai, G.; Wang, J.; Yang, L.; So, S. K.; Djurišić, A. B.; Leung, W. W.; Hao, J.; Chan, W. K.; Surya, C. Efficiency enhancement by defect engineering in perovskite photovoltaic cells prepared using evaporated PbI_2/CH_3NH_3I multilayers. *Journal of Materials Chemistry A* **2015**, *3* (17), 9223−9231.

(17) Abzieher, T.; Feeney, T.; Schackmar, F.; Donie, Y. J.; Hossain, I. M.; Schwenzer, J. A.; Hellmann, T.; Mayer, T.; Powalla, M.; Paetzold, U. W. From Groundwork to Efficient Solar Cells: On the Importance of the Substrate Material in Co-Evaporated Perovskite Solar Cells. *Adv. Funct. Mater.* **2021**, *31* (42), 2104482.

(18) Kulkarni, S. A.; Baikie, T.; Boix, P. P.; Yantara, N.; Mathews, N.; Mhaisalkar, S. Band-gap tuning of lead halide perovskites using a sequential deposition process. *J. Mater. Chem. A* **2014**, *2* (24), 9221−9225.

(19) Du, P.; Wang, L.; Li, J.; Luo, J.; Ma, Y.; Tang, J.; Zhai, T. Thermal Evaporation for Halide Perovskite Optoelectronics: Fundamentals, Progress, and Outlook. *Advanced Optical Materials* **2022**, *10* (4), 2101770.

(20) Ren, X.; Yang, Z.; Yang, D.; Zhang, X.; Cui, D.; Liu, Y.; Wei, Q.; Fan, H.; Liu, S. F. Modulating crystal grain size and optoelectronic properties of perovskite films for solar cells by reaction temperature. *Nanoscale* **2016**, *8* (6), 3816−3822.

(21) Zhou, Y.; Yang, M.; Vasiliev, A. L.; Garces, H. F.; Zhao, Y.; Wang, D.; Pang, S.; Zhu, K.; Padture, N. P. Growth control of compact $CH_3NH_3PbI_3$ thin films via enhanced solid-state precursor reaction for efficient planar perovskite solar cells. *Journal of Materials Chemistry A* **2015**, *3* (17), 9249−9256.

(22) Wu, Y.; Islam, A.; Yang, X.; Qin, C.; Liu, J.; Zhang, K.; Peng, W.; Han, L. Retarding the crystallization of PbI_2 for highly reproducible planar-structured perovskite solar cells via sequential deposition. *Energy Environ. Sci.* **2014**, *7* (9), 2934−2938.

(23) Tan, H.; Che, F.; Wei, M.; Zhao, Y.; Saidaminov, M. I.; Todorovic, P.; Broberg, D.; Walters, G.; Tan, F.; Zhuang, T.; Sun, B.; Liang, Z.; Yuan, H.; Fron, E.; Kim, J.; Yang, Z.; Voznyy, O.; Asta, M.; Sargent, E. W. Dipolar cations confer defect tolerance in wide-bandgap metal halide perovskites. *Nat. Commun.* **2018**, *9* (1), 3100.

(24) Qiu, L.; He, S.; Jiang, Y.; Son, D.-Y.; Ono, L. K.; Liu, Z.; Kim, T.; Bouloumis, T.; Kazaoui, S.; Qi, Y. Hybrid chemical vapor deposition enables scalable and stable Cs-FA mixed cation perovskite solar modules with a designated area of 91.8 cm^2 approaching 10% efficiency. *Journal of Materials Chemistry A* **2019**, *7* (12), 6920−6929.

(25) Muscarella, L. A.; Hutter, E. M.; Sanchez, S.; Dieleman, C. D.; Savenije, T. J.; Hagfeldt, A.; Saliba, M.; Ehrler, B. Crystal Orientation and Grain Size: Do They Determine Optoelectronic Properties of $MAPbI_3$ Perovskite? *J. Phys. Chem. Lett.* **2019**, *10* (20), 6010−6018.

(26) Reid, O. G.; Yang, M.; Kopidakis, N.; Zhu, K.; Rumbles, G. Grain-Size-Limited Mobility in Methylammonium Lead Iodide Perovskite Thin Films. *ACS Energy Letters* **2016**, *1* (3), 561−565.

(27) Momblona, C.; Gil-Escrig, L.; Bandiello, E.; Hutter, E. M.; Sessolo, M.; Lederer, K.; Blochwitz-Nimoth, J.; Bolink, H. J. Efficient vacuum deposited p-i-n and n-i-p perovskite solar cells employing doped charge transport layers. *Energy Environ. Sci.* **2016**, *9* (11), 3456−3463.

(28) Lu, H.; Liu, Y.; Ahlawat, P.; Mishra, A.; Tress, W. R.; Eickemeyer, F. T.; Yang, Y.; Fu, F.; Wang, Z.; Avalos, C. E.; Carlsen, B. I.; Agarwalla, A.; Zhang, X.; Li, X.; Zhan, Y.; Zakeeruddin, S. M.; Emsley, L.; Rothlisberger, U.; Zheng, L.; Hagfeldt, A.; Gratzel, M. Vapor-assisted deposition of highly efficient, stable black-phase $FAPbI_3$ perovskite solar cells. *Science* **2020**, *370* (6512), eabb8985.

(29) Zhao, J.; He, G.; Yang, D.; Guo, D.; Yang, L.; Chen, J.; Ma, D. Highly stable and efficient α-phase FA-based perovskite solar cells prepared in ambient air by strategically enhancing the interaction between ions in crystal lattices. *Sustainable Energy & Fuels* **2021**, *5* (17), 4268−4276.

https://doi.org/10.1021/acsaem.3c00203
ACS Appl. Energy Mater. XXXX, XXX, XXX−XXX